Electronic Supplementary Material (ESI) for Journal of Materials Chemistry A.


# Supporting Information

# Fe/$Fe_3C$ modification to effectively achieve high-performance Si-C anode

Xuqi Lin[1,2,3], Jingguo Gao[1,2,3], Kehua Zhong[1,2,3], Yongcong Huang[1,2,3], Hurong Yao[1,2,3], Yingbin Lin[1,2,3], Yongping Zheng[1,2,3]*, Zhigao Huang[1,2,3]*, Jiaxin Li[1,2,3]*

[1] College of Physics and Energy, Fujian Provincial Solar Energy Conversion and Energy Storage Engineering Technology Research Center, Fujian Normal University, Fuzhou, 350117, China.

[2] Fujian Provincial Key Laboratory of Quantum Manipulation and New Energy Materials, Fuzhou, 350117, China.

[3] Fujian Provincial Collaborative Innovation Center for Advanced High-Field Superconducting Materials and Engineering, Fuzhou, 350117, China.

*Corresponding author: Dr.&Prof. Jiaxin Li; Dr. Yongping Zheng; Dr.&Prof. Zhigao Huang

Tel: +86-591-2286-8132; Fax: +86-591-2286-8132

*E-mail: lijiaxin@fjnu.edu.cn; zyp@fjnu.edu.cn; zghuang@fjnu.edu.cn.

## TGA Calculation:

It is known from the Figure 3b that as the temperature increases, both show that the percentage of material decreases and then rises after a plateau, which represent the Si content of Si@CNFs and the Si and $Fe_2O_3$ content of Fe/$Fe_3C$-Si@CNFs, respectively. Meanwhile, the contents of Si@CNFs and Fe/$Fe_3C$-Si@CNFs at plateau are 42.4% and 52.7%, respectively. The falling phenomenon can be attributed to the disappearance of the carbon material, and the subsequent rising phenomenon belongs to the process of silicon oxidation. In addition, Fe/$Fe_3C$-Si@CNFs also includes the oxidation reaction of Fe in the process of material percentage decrease. Based on the above, we can calculate as follows: The proportion of SiOx in Si@CNFs accounts for 63.7% after oxidation. The equation can be listed as : $\frac{42.4}{28} = \frac{63.7}{28 + 16x}$.

The proportion of SiOx and $Fe_2O_3$ in Fe/$Fe_3C$-Si@CNFs accounts for 72.2% after oxidation. The equation can be listed as: $\frac{y}{28} = \frac{z}{28 + 16x}$

$$b + y = 52.7$$

$$b + z = 72.2$$

$$\frac{a}{56} = \frac{b}{56 * 2 + 16 * 3}$$

x- the number of atoms occupied by O in SiOx;

y- the proportion of Si in Fe/$Fe_3C$-Si@CNFs;

z- the proportion of SiOx in Fe/$Fe_3C$-Si@CNFs;

a- the proportion of Fe in Fe/$Fe_3C$-Si@CNFs;

b- the proportion of $Fe_2O_3$ in Fe/$Fe_3C$-Si@CNFs;

The proportion of Fe and Si in Fe/$Fe_3C$-Si@CNFs accounts for 39% and 4.8%, respectively.

The proportion of Si in Si@CNFs accounts for 42%.

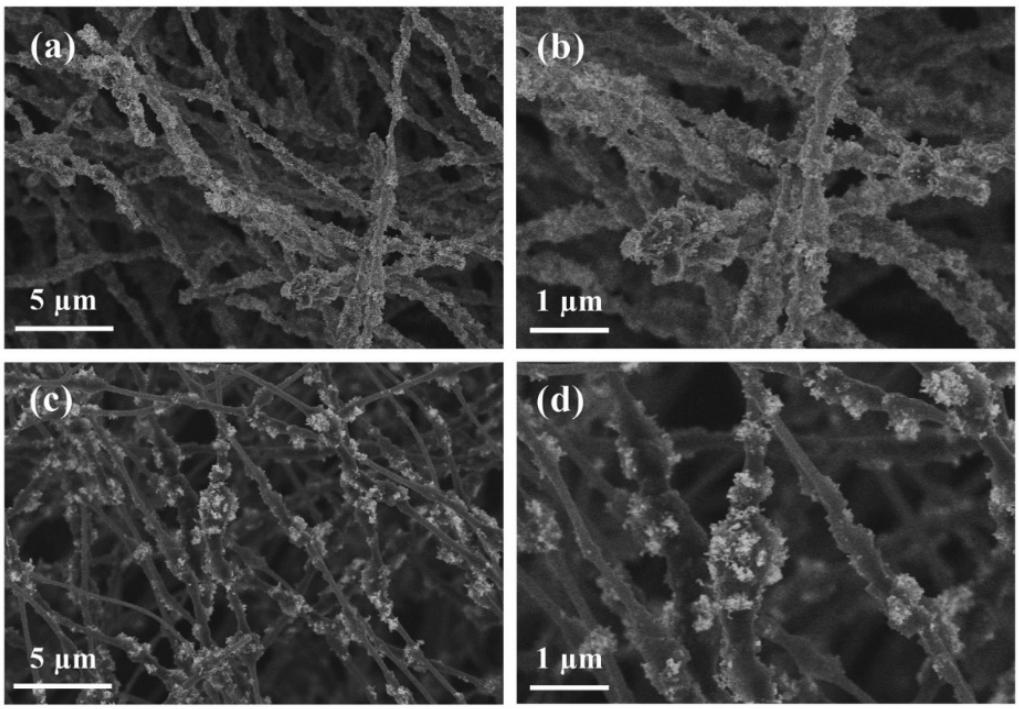


**Figure S1.** The different magnified SEM images of (a, b) Fe/$Fe_3C$-Si@CNFs and (c, d) Si@CNFs composite.

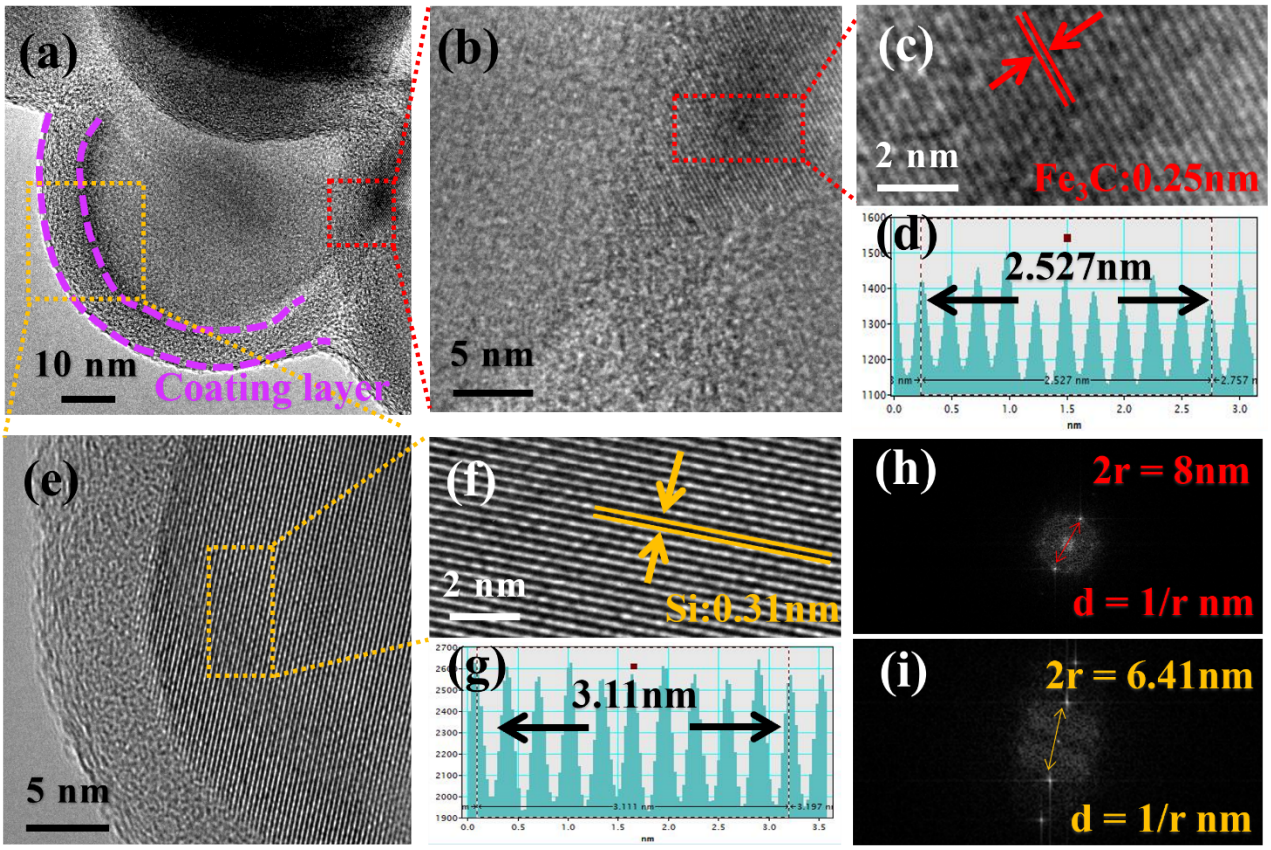


**Figure S2.** The HR-TEM images of the Fe/$Fe_3C$-Si@CNFs composite: (a, b, e) HR-TEM images; The specific position of lattice fringes, line profiles, and FFT for $Fe_3C$ (c, d, h) and Si (f, g, i).

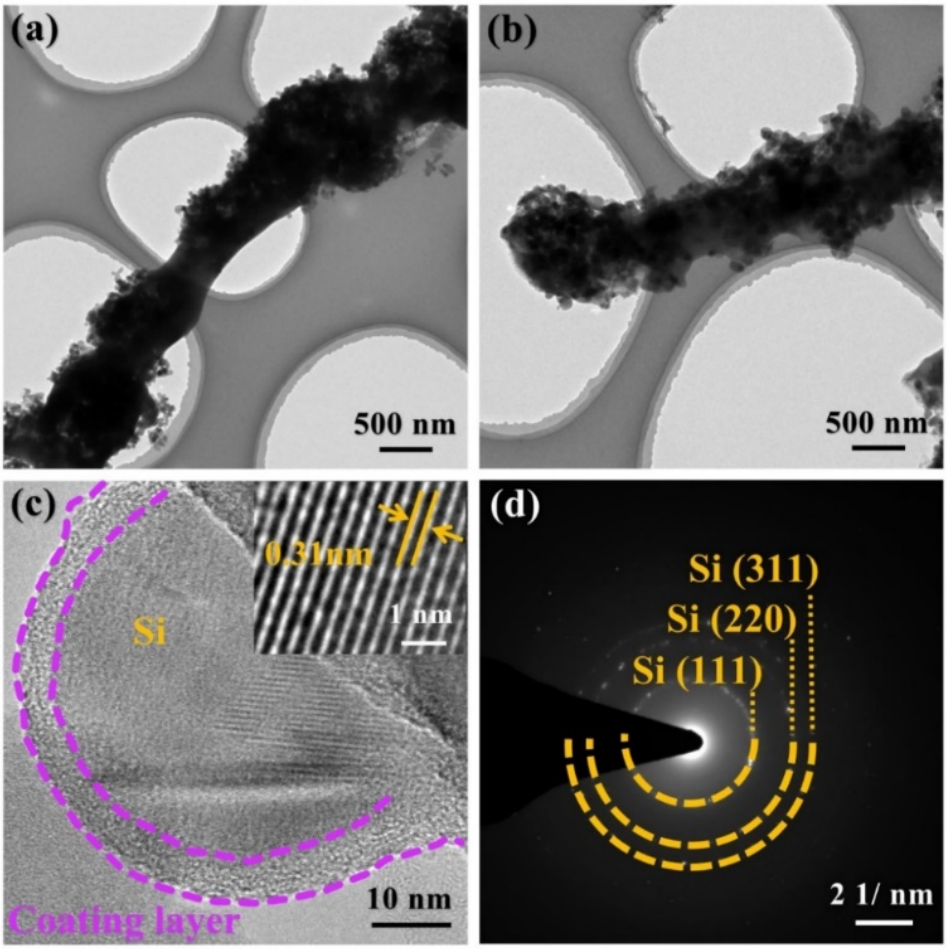


**Figure S3.** (a-b) TEM; (c) HR-TEM; (d) SAED of Si@CNFs.

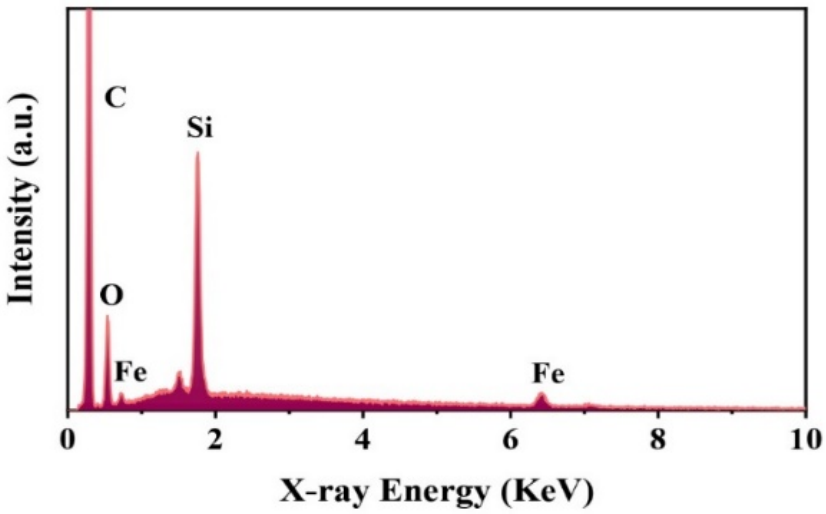


**Figure S4.** EDS spectra for $Fe/Fe_3C$-Si@CNFs.

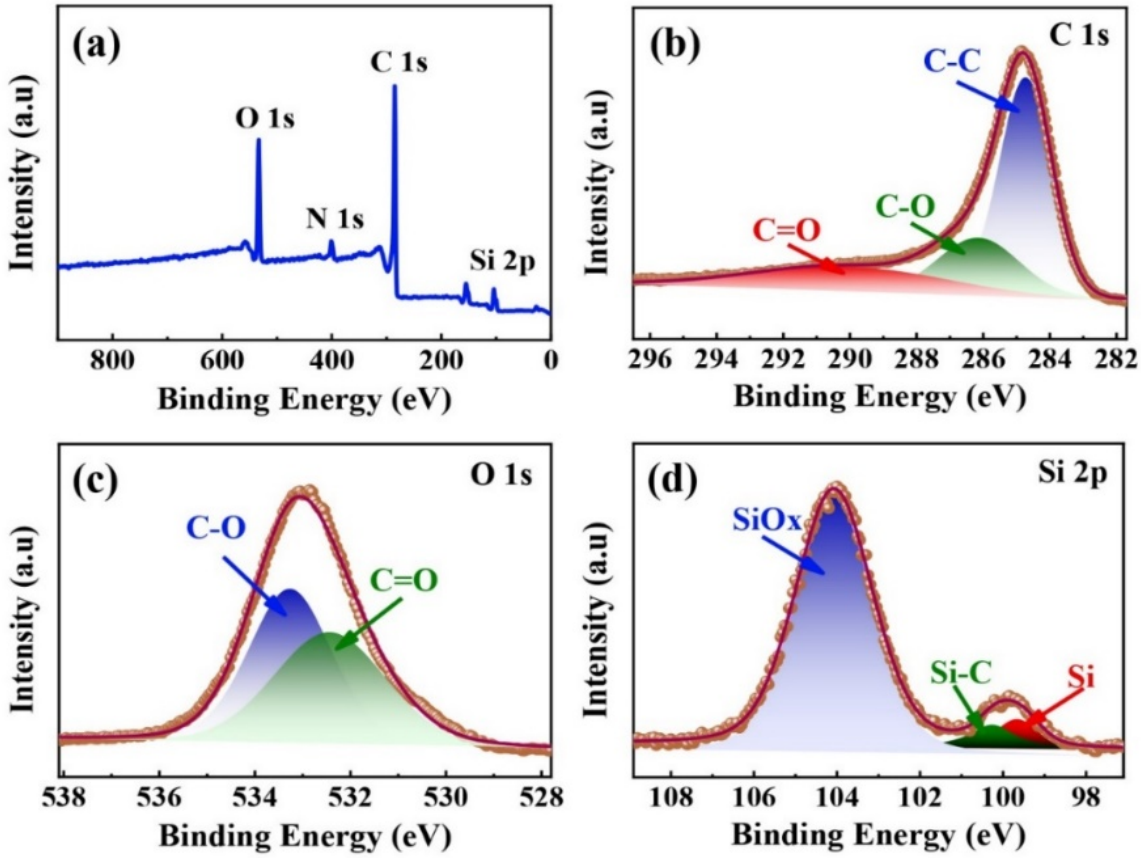


**Figure S5.** XPS full spectra and high-resolution XPS spectra of C 1s、Si 2p、O 1s for Si@CNFs.

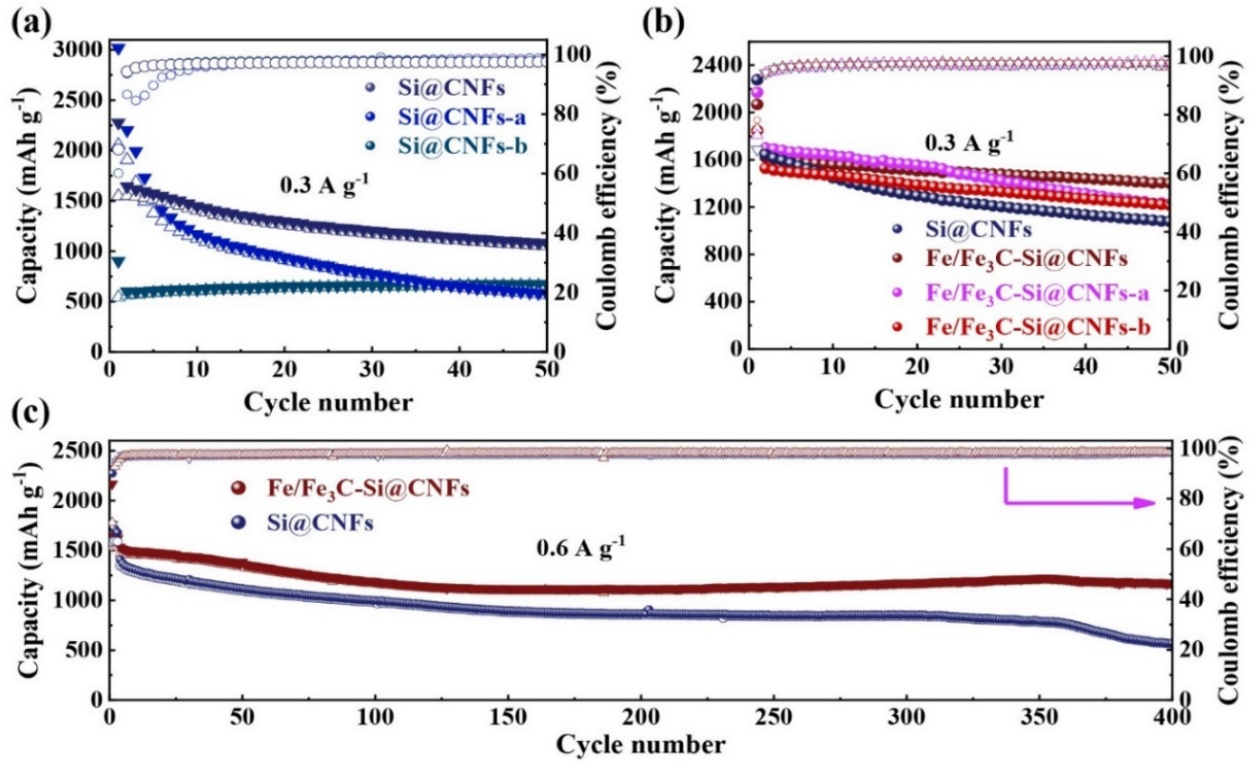


**Figure S6.** The cycle performance of Fe/$Fe_3C$-Si@CNFs and Si@CNFs anodes.

**Table S1：** PAN: Si mass ratio corresponds to the corresponding composite material

| | Si@CNFs | Si@CNFs-a | Si@CNFs-b |
|---|---|---|---|
| the mass ratio of PAN: Si | 5:2 | 5:1 | 5:3 |

**Table S2：** Si: PAN: $FeC_2O_4 \cdot 2H_2O$ mass ratio corresponds to the corresponding composite material

| | Fe/$Fe_3C$-Si@CNFs | Fe/$Fe_3C$-Si@CNFs-a | Fe/$Fe_3C$-Si@CNFs-b |
|---|---|---|---|
| the mass ratio of PAN: Si: $FeC_2O_4 \cdot 2H_2O$ | 20:8:3 | 20:8:2 | 20:8:4 |

In order to determine the optimal material ratio, we carried out many experiments based on different ratios of PAN, Si,and $FeC_2O_4 \cdot 2H_2O$ as shown in **Table S1** and **S2**. It is known from **Figure S6a** that different mass ratio for PAN: Si displays its own advantage. When the mass ratio of PAN: Si is 5:1, Si@CNFs-a shows low capacity and excellent stability and is 5:3, Si@CNFs-b displays high and dramatically reduced capacity. Interestingly, we choose the mass ratio of PAN: Si at 5:2 as the research proportion because the capacity and stability of Si@CNFs have been improved. Furthermore, the adding Fe/$Fe_3C$ with improving interface compatibility and reducing side effects can improve cycle

performance proved by **Figure S6**b. As the content of $Fe/Fe_3C$ increases, the capacity decreases, but when the mass ratio of PAN: Si: $FeC_2O_4 \cdot 2H_2O$ at 20:8:3, $Fe/Fe_3C$-Si@CNFs shows better electrochemical performance.

**Table S3**：Some cycle performances of silicon-carbon based LIBs in recent years

| Samples of silicon-carbon based | | Special capacity (mAh $g^{-1}$) | Current density (A $g^{-1}$) | Cycle number | Ref. |
|---|---|---|---|---|---|
| silicon-carbon-based | onion-like Si/C | 1391.3 | 0.2 | 400 | [1] |
| | Si-Sn@C/$Cu_3Si$–$P_{260}$ | 932 | 1.5 | 500 | [2] |
| | Si@zincone/$TiO_2$ | 753 | 2.0 | 1000 | [3] |
| | GP-Si | 1059 | 2.0 | 500 | [4] |
| | Si@ZIF-67 | 820 | 5.0 | 1000 | [5] |
| | Si@C@ZIF-67-800N | 853 | 1.0 | 300 | [6] |
| | Si/CNTs | 1275.5 | 1.0 | 400 | [7] |
| | CNTs/Si/C nanotubes | 932.2 | 2.0 | 1000 | [8] |
| | Si@10-ZC | 839 | 1.0 | 200 | [9] |
| | SiNDs@DSHC | 750 | 1.0 | 2000 | [10] |
| | CNTs@Silicon | 1152 | 0.6 | 500 | [11] |
| | Si@CNT/C microscroll | 2710 | 0.2 | 300 | [12] |
| | SF@G | ~1500 | 2.0 | 500 | [13] |
| silicon-carbon-fibers based | Si@HC/CNFs | 1076.5 | 0.2 | 100 | [14] |
| | Si@void@C NF | 1045 | 0.5 | 100 | [15] |
| | Si@MC-CNFs | 771 | 0.1 | 150 | [16] |
| | NL-Si@C-0.5 | 710 | 0.5 | 200 | [17] |
| | SHCM/NCF | 1442 | 1.0 | 800 | [18] |
| | Si@c-ZIF@CNFs | 518.6 | 1.0 | 100 | [19] |
| | Si/C-ZIF/CNFs | 538.6 | 0.5 | 500 | [20] |
| | **Fe/$Fe_3C$-Si@CNFs** | **956.5** | **2.0** | **4000** | **This work** |

## Reference:


[1] D. Wang, C. Zhou, B. Cao, Y. Xu, D. Zhang, A. Li, J. Zhou, Z. Ma, X. Chen, H. Song, One-step synthesis of spherical Si/C composites with onion-like buffer structure as high-performance anodes for lithium-ion batteries, Energy Storage Mater. 24 (2020) 312-318.

[2] Z. Dong, W. Du, H. Gu, Y. Long, C. Zhang, G. Chen, Z. Feng, W. Sun, Y. Jiang, Y. Liu, Y. Yang, J. Gan, M. Gao, H. Pan, A Unique Structural Highly Compacted Binder-Free Silicon-Based Anode with High Electronic Conductivity for High-Performance Lithium-Ion Batteries, Small Struct. 3 (2021) 2100174-2100187.

[3] J. B. Fang, Y. Q. Cao, S. Z. Chang, F. R. Teng, D. Wu, A. D. Li, Dual-Design of Nanoporous to Compact Interface via Atomic/Molecular Layer Deposition Enabling a Long-Life Silicon Anode, Adv. Funct. Mater. 32 (2022) 2109682-2109691.

[4] Z. Yang, C. Wu, S. Li, L. Qiu, Z. Yang, Y. Zhong, B. Zhong, Y. Song, G. Wang, Y. Liu, Z. Wu, X. Guo, A Unique Structure of Highly Stable Interphase and Self-Consistent Stress Distribution Radial-Gradient Porous for Silicon Anode, Adv. Funct. Mater. 32 (2021) 2107897-2107904.

[5] R. Gao, J. Tang, X. Yu, S. Tang, K. Ozawa, T. Sasaki, L.-C. Qin, In situ synthesis of MOF-derived carbon shells for silicon anode with improved lithium-ion storage, Nano Energy 70 (2020) 104444-104451.

[6] N. Liu, J. Liu, D. Jia, Y. Huang, J. Luo, X. Mamat, Y. Yu, Y. Dong, G. Hu, Multi-core yolk-shell like mesoporous double carbon-coated silicon nanoparticles as anode materials for lithium-ion batteries, Energy Storage Mater. 18 (2019) 165-173.

[7] Z. Yi, N. Lin, Y. Zhao, W. Wang, Y. Qian, Y. Zhu, Y. Qian, A flexible micro/nanostructured Si microsphere cross-linked by highly-elastic carbon nanotubes toward enhanced lithium ion battery anodes, Energy Storage Mater. 17 (2019) 93-100.

[8] R. Liu, C. Shen, Y. Dong, J. Qin, Q. Wang, J. Iocozzia, S. Zhao, K. Yuan, C. Han, B. Li, Z. Lin, Sandwich-like CNTs/Si/C nanotubes as high performance anode materials for lithium-ion batteries, J. Mater. Chem. A 6 (2018) 14797-14804.

[9] T. Mu, Y. Zhao, C. Zhao, N. G. Holmes, S. Lou, J. Li, W. Li, M. He, Y. Sun, C. Du, R. Li, J. Wang, G. Yin, X. Sun, Stable Silicon Anodes by Molecular Layer Deposited Artificial Zincone Coatings, Adv. Funct. Mater. 31 (2021) 2010526-2010534.

[10] R. Zhu, X. Hu, K. Chen, J. Dang, X. Wang, X. Liu, H. Wang, Double-shelled hollow carbon nanospheres as enclosed electrochemical reactors to enhance the lithium storage performance of silicon nanodots, J. Mater. Chem. A 8 (2020) 12502-12517.

[11] T. Ma, H. Xu, X. Yu, H. Li, W. Zhang, X. Cheng, W. Zhu, X. Qiu, Lithiation Behavior of Coaxial Hollow Nanocables of Carbon-Silicon Composite, ACS Nano 13 (2019) 2274-2280.

[12] Y. Chen, Y. Hu, Z. Shen, R. Chen, X. He, X. Zhang, Y. Li, K. Wu, Hollow core–shell structured silicon@carbon nanoparticles embed in carbon nanofibers as binder-free anodes for lithium-ion batteries, J. Power Sources 342 (2017) 467-475.

[13] H. Wang, J. Fu, C. Wang, J. Wang, A. Yang, C. Li, Q. Sun, Y. Cui, H. Li, A binder-free high silicon content flexible anode for Li-ion batteries, Energy Environ. Sci. 13 (2020) 848-858.

[14] X. Zhang, D. Wang, X. Qiu, Y. Ma, D. Kong, K. Mullen, X. Li, L. Zhi, Stable high-capacity and high-rate silicon-based lithium battery anodes upon two-dimensional covalent encapsulation, Nat. Commun. 11 (2020) 3826-3834.

[15] Y. Han, J. Zou, Z. Li, W. Wang, Y. Jie, J. Ma, B. Tang, Q. Zhang, X. Cao, S. Xu, Z. L. Wang, Si@void@C Nanofibers Fabricated Using a Self-Powered Electrospinning System for Lithium-Ion Batteries, ACS Nano 12 (2018) 4835-4843.

[16] X. Chen, P. Hu, J. Xiang, R. Zhang, Y. Huang, Confining Silicon Nanoparticles within Freestanding Multichannel Carbon Fibers for High-Performance Li-Ion Batteries, ACS Appl. Energy Mater. 2 (2019) 5214-5218.

[17] X. Kong, Y. Zheng, Y. Wang, S. Liang, G. Cao, A. Pan, Necklace-like Si@C nanofibers as robust anode materials for high performance lithium ion batteries, Sci. Bull. 64 (2019) 261-269.

[18] R. Zhu, Z. Wang, X. Hu, X. Liu, H. Wang, Silicon in Hollow Carbon Nanospheres Assembled Microspheres Cross-linked with N-doped Carbon Fibers toward a Binder Free, High Performance, and Flexible Anode for Lithium-Ion Batteries, Adv. Funct. Mater. 31 (2021) 2101487-2101498.

[19] J. Chen, X. Guo, M. Gao, J. Wang, S. Sun, K. Xue, S. Zhang, Y. Liu, J. Zhang, Self-supporting dual-confined porous Si@c-ZIF@carbon nanofibers for high-performance lithium-ion batteries, Chem. Commun. 57 (2021) 10580-10583.

[20] Y. Zeng, Y. Huang, N. Liu, X. Wang, Y. Zhang, Y. Guo, H.-H. Wu, H. Chen, X. Tang, Q. Zhang, N-doped porous carbon nanofibers sheathed pumpkin-like Si/C composites as free-standing anodes for lithium-ion batteries, J. Energy Chem. 54 (2021) 727-735.

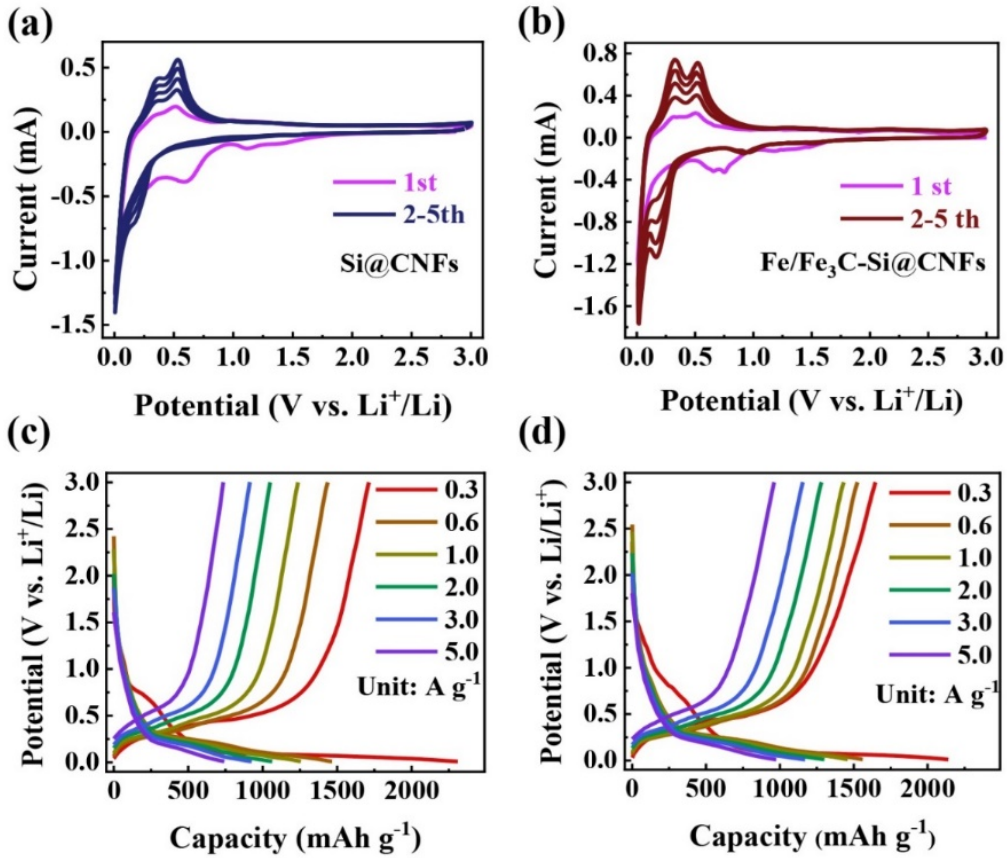


**Figure S7.** (a) CV curve at 0.2 mV $s^{-1}$ and (c) rate performance charge-discharge curves of Si@CNFs; (b) CV curve at 0.2 mV $s^{-1}$ and (d) rate performance charge-discharge curves of Fe/$Fe_3C$-Si@CNFs.

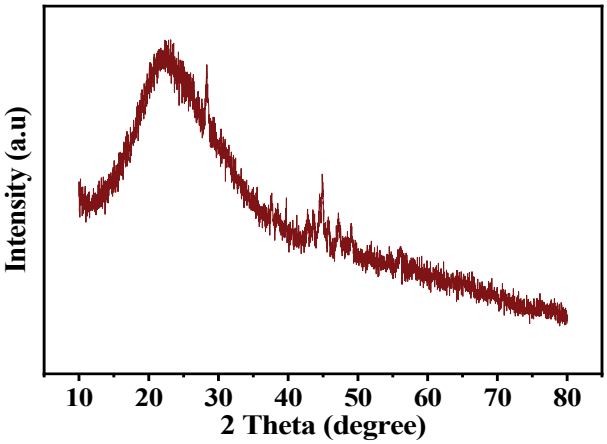


**Figure S8.** Ex-suit XRD of $Fe/Fe_3C$-Si@CNFs after 10 cycles.

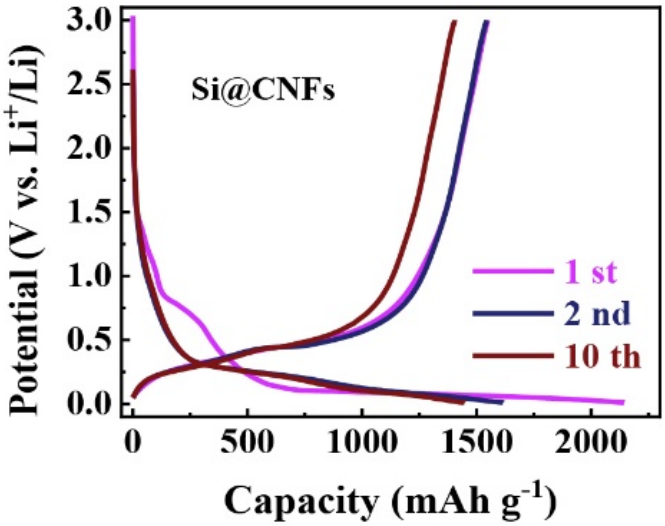


**Figure S9.** Typical discharge-charge profiles tested at 0.3 A $g^{-1}$ for Si@CNFs.

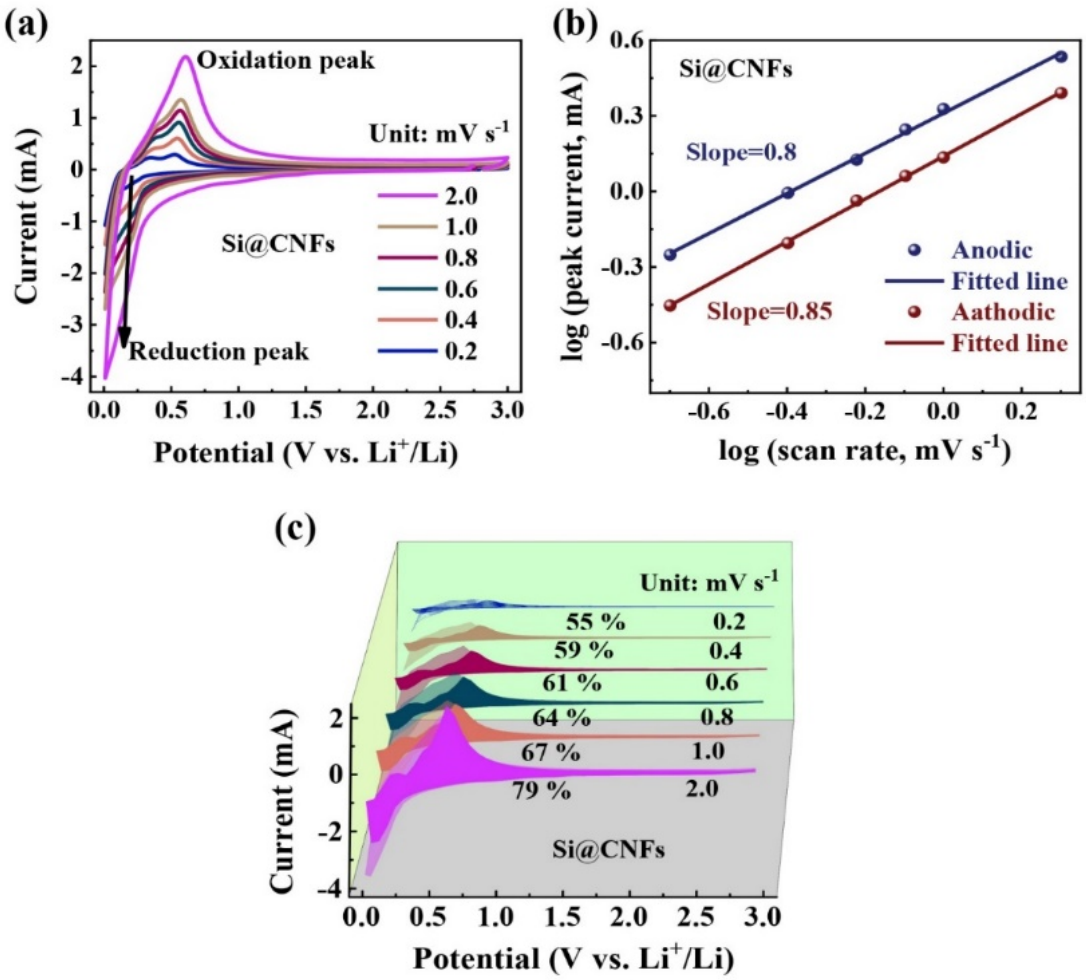


**Figure S10.** (a) CV curves at different scan rates, (b) Relationship between log(i) and log(v), and (c) Ratios of capacitance of Si@CNFs.

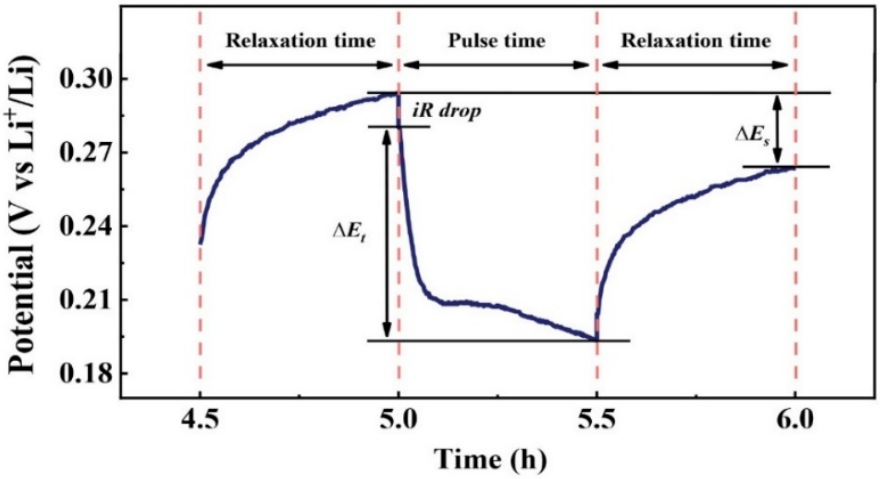


**Figure S11.** Single GITT electrode during discharge. The iR drop is shown along with the ΔEs and ΔEt.

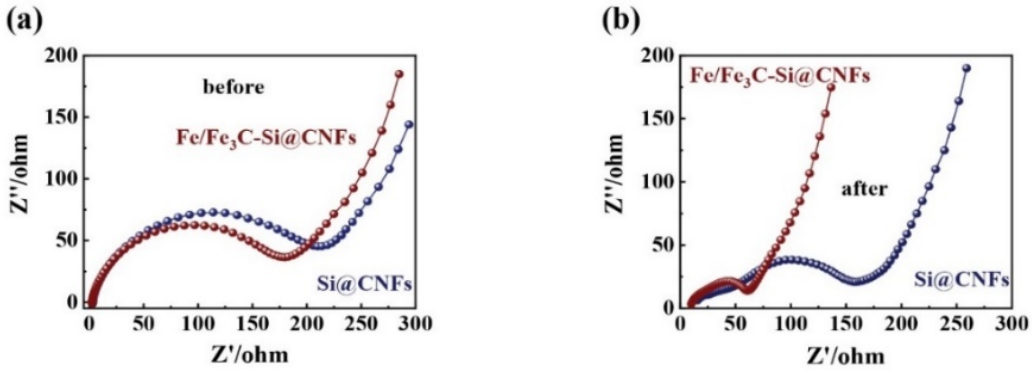


(c)

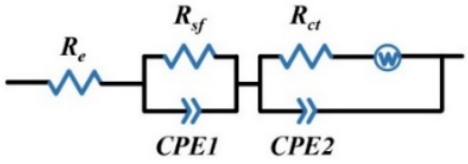


(d) After 100 cycles at 1.0 A $g^{-1}$

| | Si@CNFs | Fe/$Fe_3C$-Si@CNFs |
|---|---|---|
| $R_e$ | 8.6 | 7.8 |
| $R_{sf}$ | 50.5 | 28.3 |
| $R_{ct}$ | 150.3 | 60.5 |

**Figure S12.** The comparative electrochemical impedance spectra for Si@CNFs and Fe/$Fe_3C$-Si@CNFs: (a) before test; (b) after 100 cycles; (c) the corresponding equivalent circuit and (d) impedance parameters for **Figure S12**b.

As we know, electrochemical impedance spectroscopy (EIS) is a highly resolved electro-analytical technique that may provide unique information about the nature of electrode process related to a wide range of time constants. The EIS measurement of fresh and post cycling batteries for Si@CNFs and Fe/$Fe_3C$-Si@CNFs are displayed in **Figure S12**, revealing equivalent electrical circuit model and impedance parameters. The EIS results in **Figure S12**a show that two electrodes delivered the similar electrochemical impedance, but the Fe/$Fe_3C$ adding slightly reduce the conductance of its composite. It is known from **Figure S12**b that the overall shape of Nyquist plots for all samples are composed of three parts including two semicircles followed by a one line. According to the literature,[1-2] the high-frequency semicircle is related to Li ion migration through the SEI film covering the surface of the electrode, the middle-frequency semicircle is attributed to charge transfer through the electrode/electrolyte interface, and the steep sloping line is assigned to solid-state diffusion of the Li ions into the bulk of the electrode material. The impedance spectra are fitted with an equivalent circuit as shown in **Figure S12**c, where $R_e$ is the solution resistance, $R_{sf}$ and ***CPE1*** are the resistance and capacitance of the SEI film, respectively, $R_{ct}$ and ***CEP2*** are the charge transfer resistance at the

particle/electrolyte interface and double-layer capacitance, respectively, and $R_w$ is Warburg impedance. The $R_{ct}$ value of Fe/$Fe_3C$-Si@CNFs is evaluated as 60.5 Ω much smaller than that (150.3 Ω) of Si@CNFs, and the $R_{sf}$ value of Fe/$Fe_3C$-Si@CNFs is calculated as 28.3 Ω much smaller than that (50.5 Ω) of Si@CNFs. Smaller $R_{ct}$ and $R_{sf}$ indicate Fe/$Fe_3C$ adding could improve the electrolyte interface compatibility and suppress the accumulation of the SEI film especially at long cycle.

## Reference:


[1] S. Zhang, M. S. Ding, K. Xu, J. Allen, T. R. Jow, Understanding Solid Electrolyte Interface Film Formation on Graphite Electrodes, Electrochem. Solid-State Lett. 4 (2001) A206-A208.

[2] S.-D. Xu, Q.-C. Zhuang, L.-L. Tian, Y.-P. Qin, L. Fang, S.-G. Sun, Impedance Spectra of Nonhomogeneous, Multilayered Porous Composite Graphite Electrodes for Li-Ion Batteries: Experimental and Theoretical Studies, J. Phys. Chem. C 115 (2011) 9210-9219.

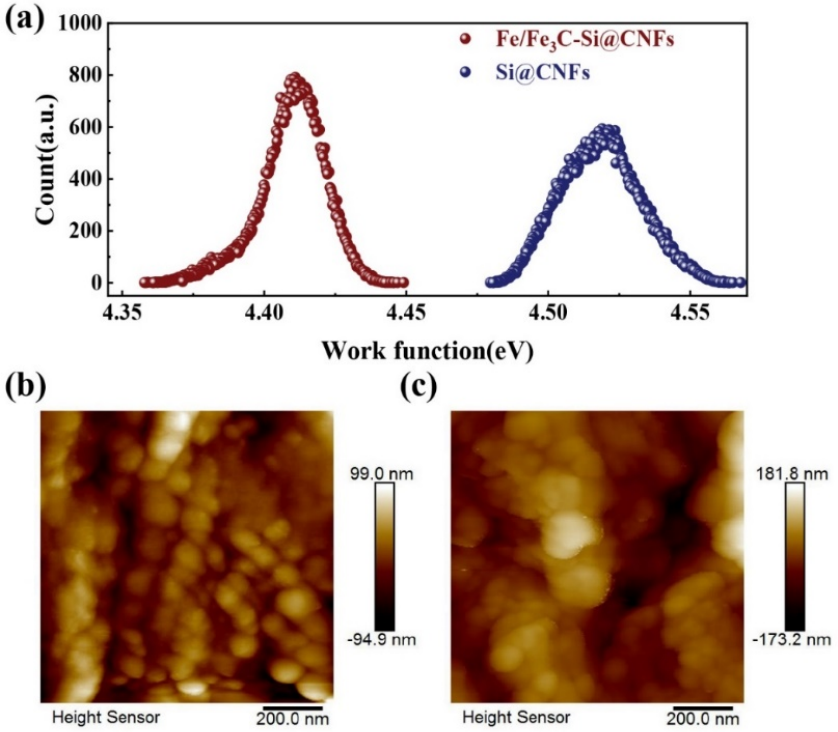


**Figure S13.** (a) the calculated work functions of Fe/$Fe_3C$-Si@CNFs and Si@CNFs; surface potential mapping of (b) Fe/$Fe_3C$-Si@CNFs and (c) Si@CNFs.

The Kelvin probe atomic force microscopy (KPFM) has been used to investigate the conductivity of electrode materials. **Figures S13**b-c present the surface potential maps of these both composites at room temperature, characterized by KPFM. the work functions for the composites of Fe/$Fe_3C$-Si@CNFs and Si@CNFs are presented in **Figures S13**a, where work function represents the minimum thermodynamic energy needed to escape an electron from the materials.[1-2] Obviously, Fe/$Fe_3C$-Si@CNFs has a smaller work function (~4.41 eV) than that (~4.52 eV) of the Si@CNFs. The smaller work function reflects the improved electron transfer in composite surface, which might be verified that the addition of Fe/$Fe_3C$ has a certain optimization effect on the interface.

## Reference:

[1] J. Li, Y. Huang, W. Huang, J. Tao, F. Lv, R. Ye, Y. Lin, Y. y. Li, Z. Huang, J. Lu, Simple Designed Micro-Nano Si-Graphite Hybrids for Lithium Storage, Small 17 (2021) 2006373-2006385.

[2] J. Tao, L. Lu, B. Wu, X. Fan, Y. Yang, J. Li, Y. Lin, Y. Y. Li, Z. Huang, J. Lu, Dramatic improvement enabled by incorporating thermal conductive TiN into Si-based anodes for lithium ion batteries, Energy Storage Mater. 29 (2020) 367-376.

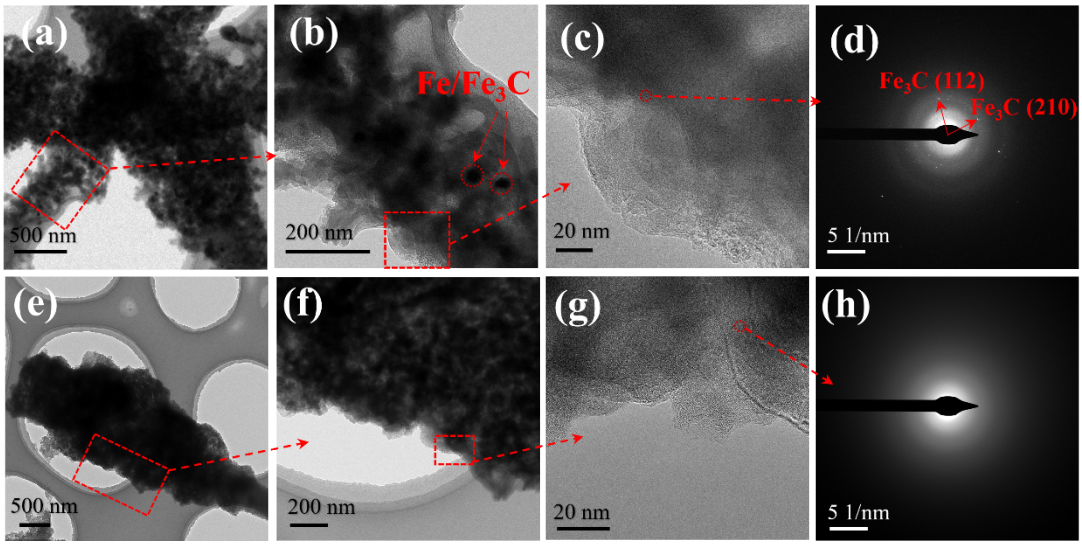


**Figure S14.** The HR-TEM and SAED of Fe/$Fe_3C$-Si@CNFs (a-d) and Si@CNFs (e-h).

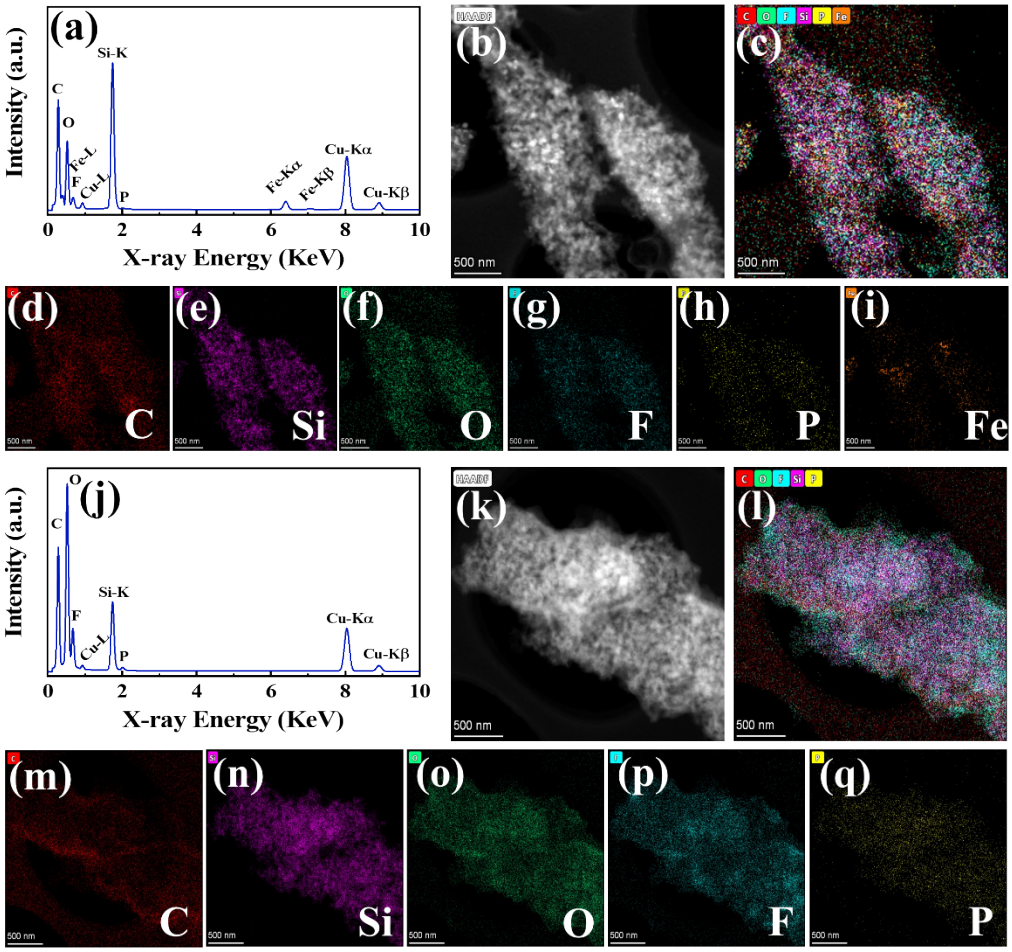


**Figure S15.** The EDS and element mapping images of Fe/$Fe_3C$-Si@CNFs (a-i) and Si@CNFs (j-q).

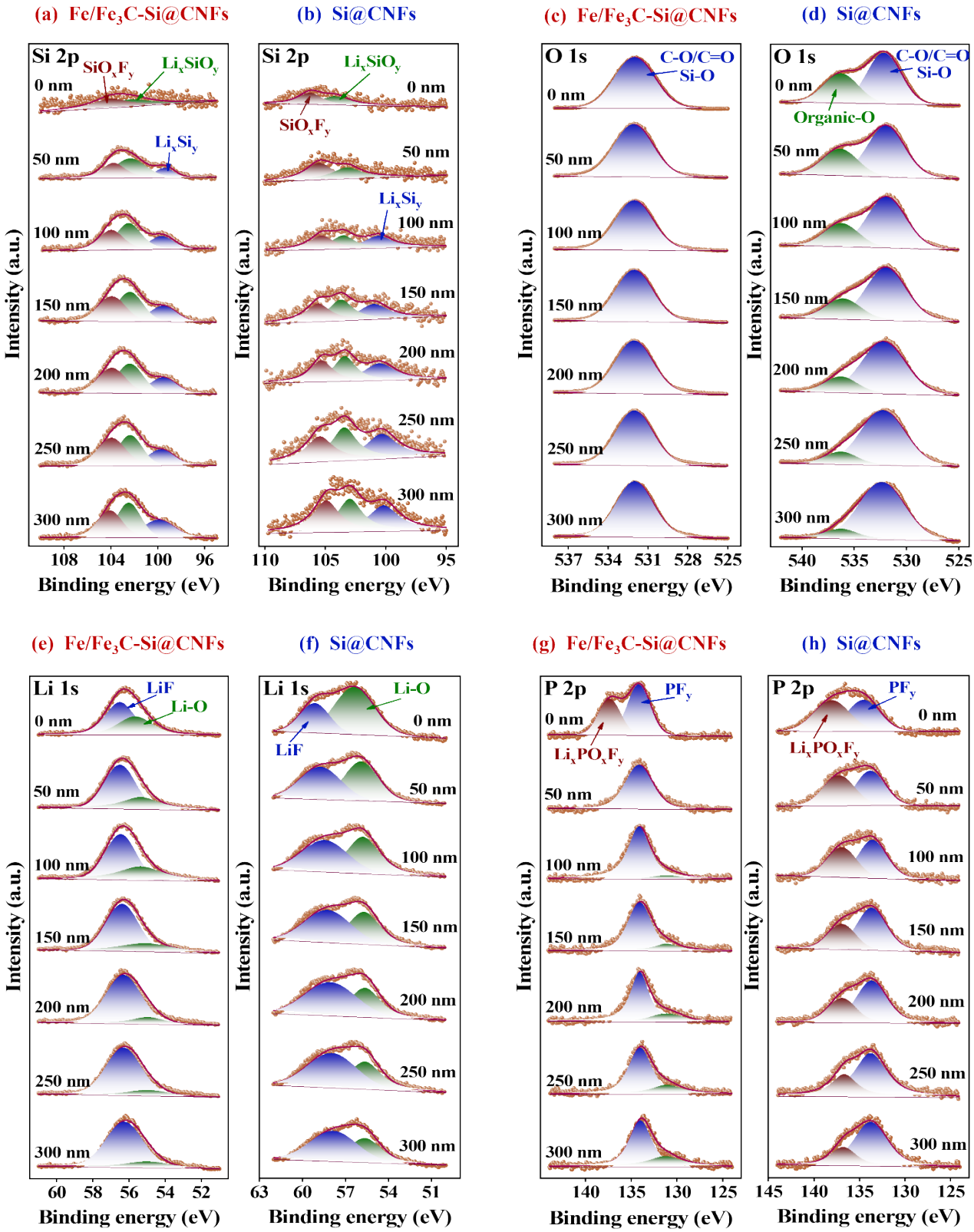


**Figure S16.** (a-h) High-resolution XPS etching curves for Fe/$Fe_3C$-Si@CNFs and Si@CNFs anodes.

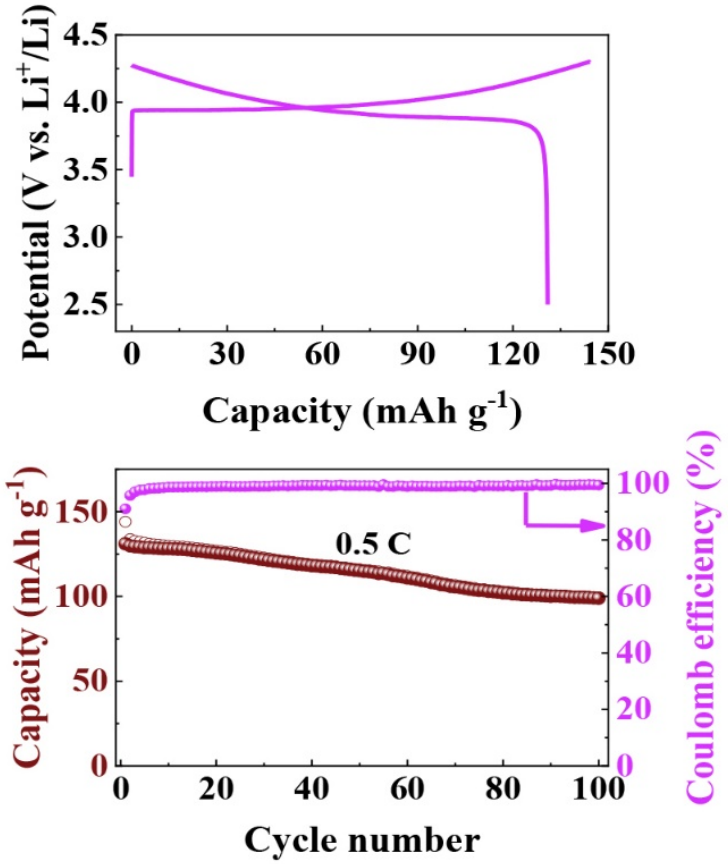


**Figure S17.** The electrochemical performance of coin-type $LCoO_2$ half-cell at 0.5C.